Computational screening of doped MnO2 catalystsfor the oxygen evolution reaction

Tripkovic, Vladimir; Hansen, Heine Anton; Vegge, Tejs

Published in:
ChemSusChem (Print)

Link to article, DOI:
10.1002/cssc.201701659

Publication date:
2018

Document Version
Peer reviewed version

CHEMISTRY & SUSTAINABILITY

CHEMSUSCHEM

ENERGY & MATERIALS

Accepted Article

Title: Computational screening of doped αMnO2 catalysts for the oxygen evolution reaction

Authors: Vladimir Tripkovic, Heine Anton Hansen, and Tejs Vegge

To be cited as: *ChemSusChem* 10.1002/cssc.201701659

Link to VoR: http://dx.doi.org/10.1002/cssc.201701659

A Journal of

ChemPubSoc Europe

WILEY-VCH

www.chemsuschem.org

Computational screening of doped αMnO_2 catalysts for the oxygen evolution reaction

Dr. Vladimir Tripkovic[1*], Dr. Heine Anton Hansen[1], Prof. Tejs Vegge[1]

[1] Department of Energy Conversion and Storage, Technical University of Denmark, DK-2800 Kgs. Lyngby, Denmark.

[*]Vladimir Tripkovic: tripce@gmail.com,
Home page: http://www.asc.energy.dtu.dk/
Phone: +45 4525 8202

Minimizing energy and materials costs for driving the oxygen evolution reaction (OER) is paramount for the commercialization of water electrolysis cells and rechargeable metal-air batteries. Using density functional theory calculations, we analyze the structural stability, catalytic activity and electronic conductivity of pure and doped αMnO_2 for the OER. As a model surface, we investigate the (110) and (100) facets, on which we identify three possible active sites: a coordination unsaturated, bridge and bulk site. We evaluate the performance of pure and Cr, Fe, Co, Ni, Cu, Zn, Cd, Mg, Al, Ga, In, Sc, Ru, Rh, Ir, Pd, Pt, Ti, Zr, Nb and Sn doped αMnO_2. At each site and for each dopant, we impose the preferred valence by adding/subtracting electron donors (hydrogens) and electron acceptors (hydroxyls). From a subset of stable dopants, we identify Pd doped αMnO_2 as the only catalyst that can outperform pristine $aMnO_2$. We also discuss approaches to increase the electron conductivity as pure αMnO_2 is a narrow band-gap material.

Keywords: oxygen evolution reaction, density functional calculations, MnO2, Structure-activity relationships.

1. Introduction

The oxygen evolution reaction (OER) is the main bottleneck in direct solar and electrocatalytic water splitting cells, and rechargeable aqueous metal-air batteries. Improving the cost-efficiency of these devices requires development of efficient, stable and cheap oxygen evolving catalysts. OER proceeds through four electron/proton transfer steps, where at least 30% of the supplied energy is dissipated as heat because the reaction needs to run above the reversible potential for oxygen evolution.[1,2] Furthermore, in acid, this minimum loss is achieved through use of active and stable,

but at the same time very costly platinum group metal catalysts.[3–7] The alkaline environment is more appealing because it permits the use of cheaper first-row transition metal (TM) oxides.[8–14]

In the following, we present a brief overview of the current status and understanding of the reaction electrochemistry on MnO_2 and its derivatives. The use of Mn compounds as OER electrocatalysts is inspired by nature, where the active center for photosynthesis (read oxygen evolution) in chloroform is the protein complex called photosystem (PS) II. PS II consists of Mn_4O_4Ca cubane-like moieties enclosed by large protein chains.[15] The underlying idea for studying Mn compounds is to make an inorganic analogue to PS II, but with a higher concentration of active sites to drive the OER at a macroscopic rate. The choice of Mn is further supported by its non-toxicity, abundance, rich and versatile redox chemistry and the ability to form mixed oxides with different Mn valences.[16] The usual Mn valence in sediments and rocks ranges from +2 to +4, including their mixtures.[16] In neutral and alkali solutions, Mn undergoes a change from Mn^{2+} in Mn_3O_4, over Mn^{3+} in Mn_2O_3, to Mn^{4+} in MnO_2 in the potential range from 0 to approximately 1.0 V vs. the Reversible Hydrogen Electrode (RHE), which is the electrode scale used in this work for referencing potentials.[17] At potentials above 1.2 V *vs* RHE, MnO_2 starts to dissolve.[18] There are dozens of MnO_2 polymorphs (α, β, γ, δ, λ, ε etc.) with similar heats of formation that crystallize in different crystal structures.[19,20] The most prominent are: αMnO_2 (cryptomelane) with an orthorhombic unit cell, tetragonal β-MnO_2 (pyrolusite) with a rutile structure and layered δ-MnO_2 (birnessite), which is very similar in structure to a family of Co and Ni layered double hydroxides.[21,22] Among the different polymorphs, αMnO_2 is ostensibly the most active for the OER.[23–25] Furthermore, as it is also catalytically active for the reverse oxygen reduction reaction (ORR),[14,23,25–31] it is regarded as one of the most promising bi-functional catalysts for use in secondary metal-air batteries and reversible alkaline fuel(electrolyser) cells. What distinguishes αMnO_2 from the other MnO_2 polymorphs are the large voids (2x2 tunnels) enclosed by edge- and corner-shared MnO_6 octahedra.[16] The tunnels extend throughout the material, exposing the entire surface area to the electrolyte. The large surface area and the open structure also makes αMnO_2 a potentially interesting material for pseudo-capacitors[32,33] and intercalation electrodes in metal-air batteries.[34,35]

On the basis of the current understanding, Mn^{3+} is critical for enhancing the OER[36–39] and ORR[29] activities. The mixed valences at the surface provide near-optimal binding energies for different reaction intermediates ($^*OH$, $^*O$ and $^*OOH$); thereby reducing the reaction overpotential.

For a more detailed discussion about the catalytic role of Mn^{3+}, we refer to a recent review article.[29] The mixed Mn valences can be introduced *via* oxygen vacancies,[40,41] controlled doping[41,42], addition of an electronegative material,[43,44] or by intercalation of electrolyte ions inside the αMnO_2 tunnels.[45–47] Oxygen vacancies are introduced during synthesis under reducing conditions; however, it is highly unlikely that the vacancies can withstand highly oxidizing OER conditions during long term operation.[48]

The work is organized in the following way. First, we compute bulk properties (magnetic structure and lattice constants) and make the (110) and (100) slabs. We tune the valence of Mn and dopant ions at different sites by adding hydroxyl groups and/or adding/removing hydrogen atoms. Subsequently, we investigate possible reaction mechanisms and identify those with minimum reaction overpotentials on pure αMnO_2. We perform stability analysis for the doped catalysts and calculate reaction overpotentials for sites that featured lowest overpotential on pure αMnO_2. Finally, we discuss how the bulk electronic conductivity can be improved.

2. Theory

For total energy calculations we used the planewave Vienna ab initio Simulation Package[49] (VASP) code (version 5.3.2) with the projector augmented-wave (PAW) pseudopotentials and the PBE[50] exchange-correlation functional. For the energy calculations, we choose default pseudopotentials, except for Sr, Ba, Zr and Nb, where we use Sr_sv, Ba_sv, Zr_sv and Nb_sv in which the 2s and 4s electrons are not 'frozen' in the core, but treated as valence electrons. For calculating density of states (DOS), we used the Mn_sv pseudopotential, which provides a sharper electron energy distribution. We set the energy cutoff to 500 eV, which is 100 eV higher than the most demanding O PAW pseudopotential, among the considered elements. We represent the bulk αMnO_2 as an 8 formula unit ring repeated twice along the length of the channels. αMnO_2 is modelled as an antiferromagnetic crystal, in which face- and corner-shared Mn ions have the same and opposite magnetic moments, respectively. The (110) slab is modeled without protruding Mn ions and consist of 3 layers, where the bottom layer is kept fixed to represent the bulk crystal. The (100) slab is modeled as a 4 layer slab, with two bottom layers fixed. We add ~14 Å of vacuum to decouple the electrostatic interactions between neighboring slabs. We used the 2x2x8 Monkhorst Pack k-point grid for the bulk, 2x4x1 for the (100) and 3x4x1 for the (110) surface calculations. All calculations are performed as spin-polarized. We apply the on-site Hubbard U correction to the metal d orbitals. We use U_{eff}, defined as a difference between screened Coulomb and exchange

parameter, U_{eff} = U – J.[51] For Mn we set the U value to 2.85 eV, which is in between the U values for Mn^{2+} oxidation to Mn^{3+} (3.10 eV) and Mn^{3+} to Mn^{4+} (2.60 eV). We take the average value as we expect in a full thermodynamic evolution cycle to have ions in the +2, +3 and +4 oxidation state. As the U values are quite similar, we do not expect the choice of U to have significant influence on the reaction energetics. We relax the structures until the forces are below 0.05 eV/Å.

$$MnO(s) + ½O_2(g) \rightarrow MnO_2(s) \qquad \text{Eq. (1)}$$

$$\alpha Mn_2O_3(s) + ½O_2(g) \rightarrow MnO_2(s) \qquad \text{Eq. (2)}$$

Formation energies of doped αMnO_2 are computed against the most stable individual host and dopant oxides at 1.7 V vs. RHE, unless otherwise stated. In the case of TM dopants, we choose oxide references such that the TM valence in the oxide is the same as in doped αMnO_2. Cr_2O_3, Fe_2O_3, CoO_2, NiO_2, CuO, ZnO, CdO, MgO, Al_2O_3, Ga_2O_3, In_2O_3, Sc_2O_3, RuO_2, RhO_2, IrO_2, PdO_2, PtO_2, TiO_2, ZrO_2, Nb_2O_5 and SnO_2 are used as references for the respective metals. It is noteworthy that ZnO, CdO, Al_2O_3, Ga_2O_3, In_2O_3, RuO_2, IrO_2 and SnO_2 are amphoteric oxides, which might limit the use of respective metals in highly alkaline environments. Different sites have different local geometries depending on the preferred oxidation state of the dopant atom. In the case of Cr and Fe, Cr_2O_3 and Fe_2O_3 are taken as references because these are the most stable oxides, albeit at OER conditions, both Cr and Fe are stable as dissolved FeO_4^{2-} and CrO_4^{2-} ions. The expression for calculating the heats of formation depends on the dopant valence and the active site. At coordination unsaturated sites (cus) on the (110) surface, formation energies for di- (M = Mg, Cu, Zn and Cd), tri- (M = Cr, Fe, Al, Ga, In and Sc), tetra- (M = Co, Ni, Ru, Rh, Ir, Pd, Pt, Ti, Zr and Sn) and pentavalent (M = Nb) dopants are calculated through Eqs. (3) – (6).

divalent: $\Delta G_d = E(Mn_{x-1}M_1O_{2x+1}H_4) - E(Mn_xO_{2x+2}H_4) + E(MnO_2) - E(MO)$ Eq. (3)

trivalent: $\Delta G_d = E(Mn_{x-1}M_1O_{2x+1}H_3) - E(Mn_xO_{2x+2}H_4) + E(MnO_2) - ½E(M_2O_3) + ½E'(H_2O)$ Eq. (4)

tetravalent: $\Delta G_d = E(Mn_{x-1}M_1O_{2x+2}H_4) - E(Mn_xO_{2x+2}H_4) + E(MnO_2) - E(MO_2)$ Eq. (5)

pentavalent: $\Delta G_d = E(Mn_{x-1}M_1O_{2x+2}H_3) - E(Mn_xO_{2x+2}H_4) + E(MnO_2) - ½E(M_2O_5) + ½E'(H_2O)$, Eq. (6)

where the number of oxygens beyond stoichiometric 2x and hydrogens beyond 0 come from addition/subtraction of hydroxyl and hydrogen atoms (*vide supra*), e.g. $Mn_xO_{2x+2}H_4$ is the stoichiometry of the MnO_2 (110) slab in equilibrium with the environment at OER conditions. $E'(H_2O) = E(H_2O) - T\Delta S(H_2O)$, in which $E(H_2O)$ and $T\Delta S(H_2O)$ are the computed electronic energy and entropy of a water molecule, respectively. We make several standard assumptions in eqs. (3-10). We assume that zero-point energies do not change for the same element in different compounds. We take 0 entropy for solids and 0.67 eV[1] for water.

The corresponding equations at the bridge (110) site are:

$$\Delta G_d = E(Mn_{x-1}M_1O_{2x+2}H_6) - E(Mn_xO_{2x+2}H_4) + E(MnO_2) - E(MO) - E'(H_2O) \quad \text{Eq. (7)}$$

$$\Delta G_d = E(Mn_{x-1}M_1O_{2x+2}H_5) - E(Mn_xO_{2x+2}H_4) + E(MnO_2) - \tfrac{1}{2}E(M_2O_3) - \tfrac{1}{2}E'(H_2O) \quad \text{Eq. (8)}$$

$$\Delta G_d = E(Mn_{x-1}M_1O_{2x+2}H_4) - E(Mn_xO_{2x+2}H_4) + E(MnO_2) - E(MO_2)$$
Eq. (9)

$$\Delta G_d = E(Mn_{x-1}M_1O_{2x+2}H_3) - E(Mn_xO_{2x+2}H_4) + E(MnO_2) - \tfrac{1}{2}E(M_2O_5) + \tfrac{1}{2}E'(H_2O). \quad \text{Eq. (10)}$$

Imposing the same dopant ion valence in the reference oxide and αMnO_2 warrants a relatively small dependence of formation energies on the U-values. For Cr, Fe, Co, Ni, Cu and Pt metals, we used U = 5, 5, 4, 3.2, 5 and 1 eV, respectively from a previous study.[22]

3. Results and discussion

We use the structural stability, catalytic activity and electronic conductivity as selection criteria to pinpoint the best doped electrocatalysts. Such a systematic approach assumes that all fundamental requirements of a good electrocatalyst are taken into account.

3.1. Pristine

3.1.1. Stability

As model surfaces, we select the low index (110) and (100) terminations, [25,35] wherein we remove protruding Mn atoms at the (110) slab to obtain two different surface sites, a cus and a bridge site. The same sites appear if the crystal is cleaved along the (100) plan and are also present on close-packed terminations of other MnO_2 polymorphs.[52] In addition to the cus and bridge site, there is

also a bulk site. Here, we use the 'bulk' label to denote all subsurface sites. In reality, the bulk sites are also accessible to reactants through large 2x2 tunnels that permeate the structure.

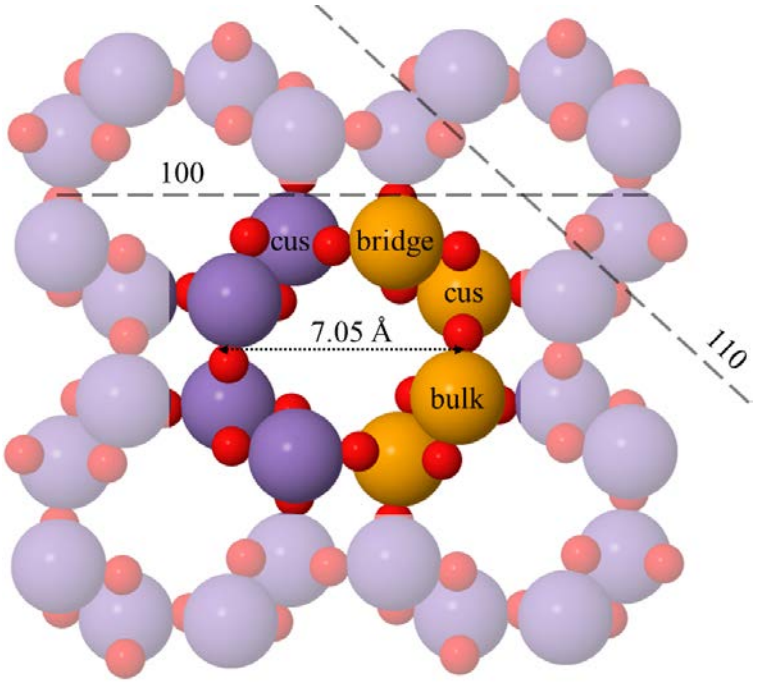

Figure 1 a) Illustration of the bulk αMnO$_2$ showing three different doping sites. Dashed lines indicate the (110) and (100) cleavage planes. Opaque atoms form the bulk and the (100) surface unit cell, whereby orange atoms make the simulated (110) slab.

Prior to computing formation energies, it is important to adjust the surface to account for desired valence of Mn ions, which at OER conditions is 4.[53] On a pure MnO_2 surface, the nominal valence at each site can be calculated by counting the average number of electrons withdrawn by Mn ions from its ligands using the

$$valence = \sum_j^k \frac{\sum_i^n n_e^-}{CN_j}, \qquad (11)$$

formula, where CN stands for the coordination number, i.e. the number of Mn ions to which a ligand ion is bound. The n sum is over ligands with the same CN and the k sum is over ligands with different CN. We illustrate the use of Eq. (11) by several examples.

10.1002/cssc.201701659

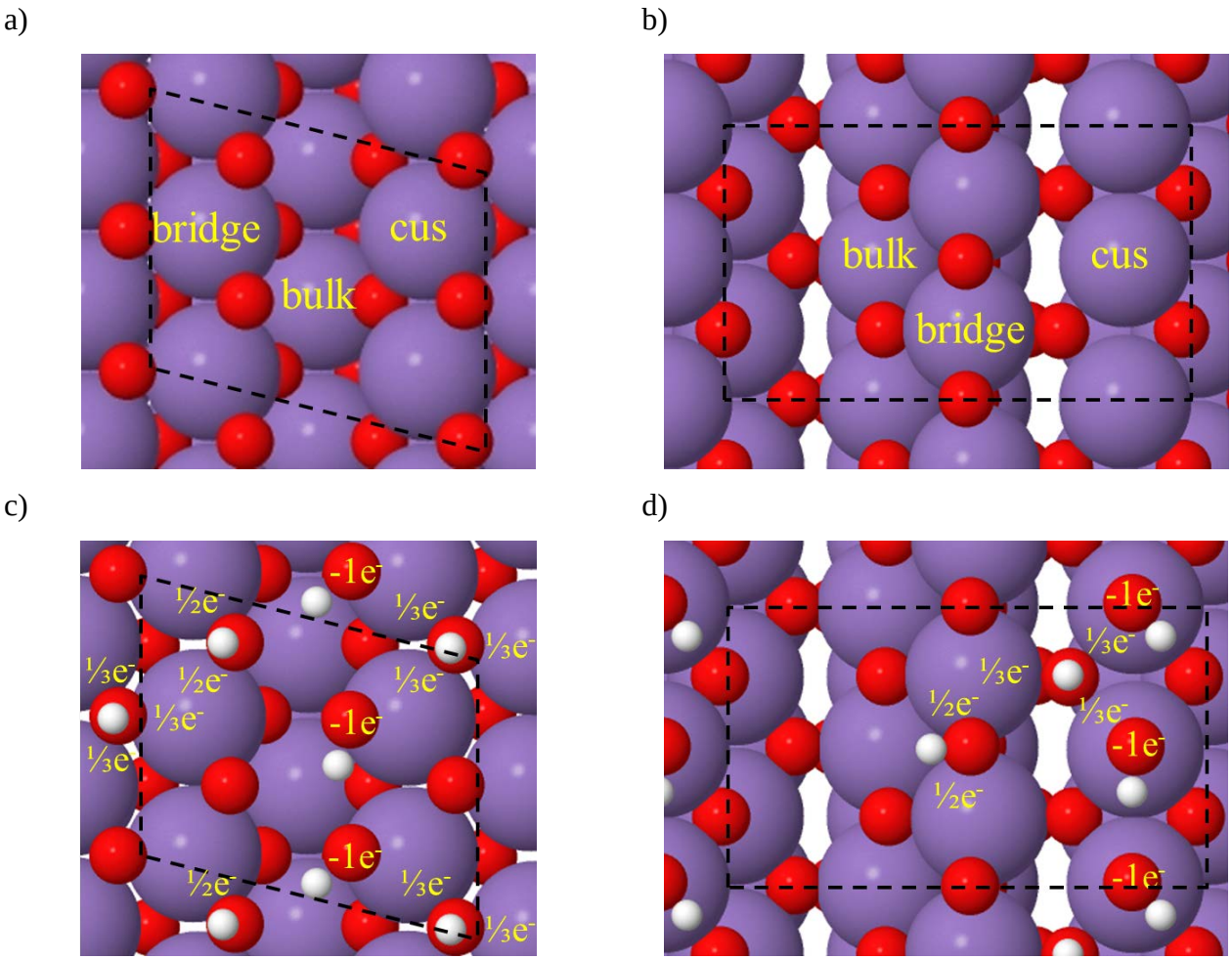

Figure 2 Top views of the (110) and (110) surfaces as cleaved (a & b) and after adjusting the surface Mn ion valence (c & d). The relative amount of charge supplied by adding electron acceptors (hydroxyls) and electron donors (hydrogens) to surface Mn ions are denoted by negative and positive values, respectively. Surface unit cells are denoted by black dashed lines.

For the bulk site, each atom is octahedrally coordinated to 6 oxygen ligands. This yields in total $2^{*}6$ electrons distributed over three neighboring Mn sites (CN = 3). Eq. (11) gives an average number of $2^{*}6/3 = 4$ electrons withdrawn from each Mn atom, yielding a nominal oxidation state of +4. At the cus and bridge site, the situation is more complicated. At cus sites, there are 5 oxygen ligands per Mn atom, where each oxygen is shared among three Mn atoms (CN = 3), giving the average $5^{*}2/3 = 3.33$ valence. On the bridge site, there are four oxygen ligands coordinated to 3 Mn atoms (CN = 3) and two oxygen ligands coordinated to two Mn atoms (CN = 2). Thus the average

valence is $4^{*}2/3 + 2^{*}2/2 = 4.67$. To approach the nominal 4 valence at cus site, a hydrogen atom is added to an oxygen ligand coordinated to cus Mn and an OH on-top of the cus site (cf. Figure 2c). The oxygen ligand is shared among two cus and one bridge Mn ion such that each ion gets a 0.33 e^{-} portion of charge as a result of hydrogenation. The addition of hydrogen and OH changes the valence of Mn cus site to $(5^{*}2\text{-}1)/3 + 1 = 4$ according to Eq. (11). Similarly, at the bridge site, we add a hydrogen atom on a bridging oxygen ligand, such that each site receives half of an electron and changes the valence to 4.17 (cf. Figure 2d). There are two inequivalent bridge sites with nominal valences of 4.17 and 3.83 because the one Mn bridge ion receives the $⅓e^{-}$ charge from the cus site. Overall, we have added 2OH and 2H species in the simulated cell to adjust the surface Mn ion valence. This is identical to dissociating 2 water molecules on the surface. To test whether this is the most stable Mn surface, we have calculated the differential binding free energy for dissociating two water molecules (see Note 1 in the Electronic Supplementary Information, ESI). For the dissociation of the first and second water molecule we obtained values of -0.32 eV and 0.04 eV, respectively. The dissociation of the second water molecule is slightly energetically unfavorable but we expect the OH moiety to become more stable by taking the stabilizing effect of water and van der Waals interactions into account, which are not included in the simulations.[54,55] We use Eq. (11) and the same rationale to find the equilibrium structure at the (100) termination (cf. **Figure 2**b & d). In brief, we add hydroxyls on-top of cus sites, a hydrogen atom to an oxygen ligand at the bridge site and a hydrogen to a 3-fold coordinated oxygen between the bridge and cus Mn ion. Similarly as in the case of the (110) termination, the valence at Mn cus site is exactly 4, whereas there are two inequivalent bridging Mn ions, with average valences of 3.83 and 4.17, respectively.

3.1.2. Activity

3.1.3. Pristine αMnO_2

There are multiple reaction pathways for evolving oxygen, which can be classified according to the surface termination, active site and reaction mechanism (cf. **Figure 3**). The reaction can take takes place either at a single site or can involve two adjacent surface sites.

10.1002/cssc.201701659

a) b)

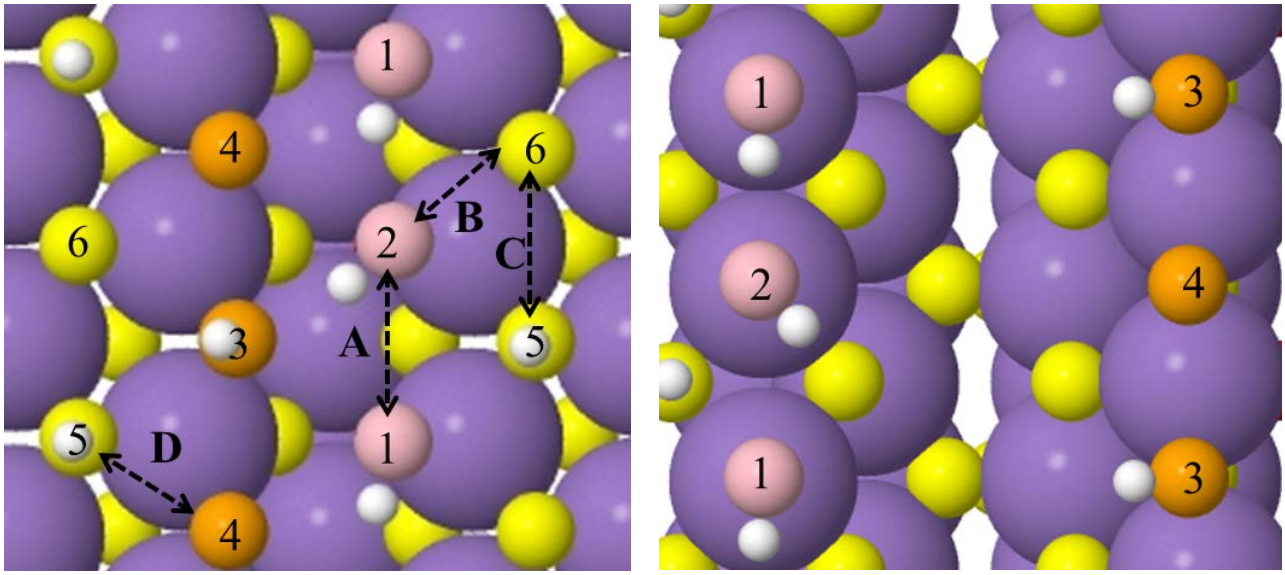

Figure 3 Different sites for oxygen evolution at the a) (110) and b) (100) αMnO$_2$ surface. The reaction can involve a single site or two adjacent sites. Oxygen ligands are colored according to their coordination; 3-fold (yellow), 2-fold (orange) and 1-fold (pink). A, B, C and D dashed lines indicate associative pathways for oxygen moieties on the (110) surface.

We assess OER activities by calculating reaction overpotentials and thermochemical barriers for O_2 desorption using adsorption free energies of reaction intermediates in their preferred binding configuration. This is an approximative, commonly employed method for comparing activities of different catalysts.[22,56,57] Under real operating conditions at which OER runs, the system is out of equilibrium and the reaction rate is controlled by the reaction kinetics. Making an exhaustive kinetic study requires calculating all possible binding configurations and coverages of different intermediates as well as barriers for proton transfer and O_2 bond formation. However in many cases the full kinetic model can be simplified by a much simpler thermodynamic model because the potential determining step (PDS) is commonly controlling the reaction rate.[58,59]

We start the analysis by examining single 1-6 sites on the modified (110) surface. At site 1, the reaction starts by dehydrogenation of the hydroxyl surface moiety (Step 1). In the second step the surface *O is hydroxylated to *OOH,[1] followed by the third step in which *OOH is deprotonated to $^*O_2$, which then leaves the surface through a potential independent step (Step 4), leaving a surface oxygen vacancy behind. Step 5 closes the thermodynamic cycle and restores the initial surface.

[1] Asterisk denotes an adsorbed intermediate or if it stands alone an empty surface site.

$^{*}OH + OH^{-}_{(aq)} \rightarrow {}^{*}O + H_2O + e^{-}$ (Step 1)

$^{*}O + OH^{-}_{(aq)} \rightarrow {}^{*}OOH + e^{-}$ (Step 2)

$^{*}OOH + OH^{-}_{(aq)} \rightarrow {}^{*}O_2 + H_2O + e^{-}$ (Step 3)

$^{*}O_2 \rightarrow {}^{*} + O_{2(g)}$ (Step 4)

$^{*} + OH^{-}_{(aq)} \rightarrow {}^{*}OH + e^{-}$ (Step 5)

The chemical step (Step 4) is often disregarded under the assumption that $^{*}O_2$ is in equilibrium with O_2(g). Step 4 will become rate limiting if the O_2 desorption barrier is prohibitive.

The same proposed electrochemical cycle holds for sites 2, 5 and 6, albeit the order of steps might not necessarily be the same. For instance, if the reaction starts on an oxygen ligand (e.g. site 2), the first step in the thermochemical cycle is Step (2) and the last Step (1). It should be noted that the sequence of steps has no effect on the computed activity parameters.

As examples of oxygen evolution pathways involving a chemical coupling step, henceforth referred to as dual-site pathways, we take the reaction on sites 1-2 and 3-4. The dual site pathway is only relevant if it circumvents the PDS at single-sites with a step that is lower in free energy. On sites 1 and 2, the PDS is Step 2, (see Note 2 in ESI), which can be by-passed if oxygen atoms at site 1 and 2 combine to make O_2 (path A in Figure 3). A second dual-site pathway that involves sites 3-4 will become feasible if it by-passes the PDS on site 3, i.e. Step (1). This will happen only if two $^{*}OH$ intermediates at sites 3 and 4 couple directly to form hydrogen peroxide intermediate, $^{*}OHOH$ (path C). If water oxidation proceeds directly to O_2, the overall reaction writes as:

$2\,{}^{*}OH \rightarrow {}^{*}OHOH + {}^{*}$ (Step 6)

$^{*}OHOH + OH^{-}_{(aq)} + {}^{*} \rightarrow {}^{*}OOH + H_2O + {}^{*} + e^{-}$ (Step 7)

$^{*} + {}^{*}OOH + OH^{-}_{(aq)} \rightarrow {}^{*} + {}^{*}O_2 + H_2O + e^{-}$ (Step 8)

$^{*}O_2 + {}^{*} \rightarrow 2^{*} + O_{2(g)}$ (Step 4)

$2^{*} + OH^{-}_{(aq)} \rightarrow {}^{*}OH + {}^{*} + e^{-}$ (Step 9)

$^{*}OH + {}^{*} + OH^{-}_{(aq)} \rightarrow 2\,{}^{*}OH + e^{-}$ (Step 10)

If the potential is above the potential for peroxide evolution, 1.77 V, water can also partially oxidize to HOOH. In that case, the reaction proceeds through

$$2^{*}OH \rightarrow {}^{*}OHOH + {}^{*} \qquad \text{(Step 6)}$$

$${}^{*}OHOH + {}^{*} \rightarrow OHOH_{(aq)} + 2^{*} \qquad \text{(Step 11)}$$

, followed by Step 9 and 10. It should be noted that the peroxide evolution reaction (PER) can only happen under the condition: $\eta_{PER} + 0.44\ V < \eta_{OER}$, where η is the reaction overpotential and 0.44 V is the difference in reversible potentials for the OER (1.23 V) and PER (1.77 V). If the above condition is not satisfied, the complete water oxidation prevails over the partial oxidation irrespective of potential. There are other dual-site pathways that involve association of OH from a cus site and a nearby oxygen ligand (path B) or association of 2 and 3-fold oxygen ligands at the bridge site (path D). Illustrations of the final states in the different associative paths are shown in Note 3 in the ESI.

From the high energy differences between the initial and final states for the A, B, C and D pathways, we conclude that coupling reactions never take place on αMnO_2. This suggests that OER takes place at single sites only with no peroxide evolution. In contrast, the reverse peroxide decomposition reaction should be very facile below its reversible potential of 0.7 V, which was in fact observed in many electrochemical measurements on MnO_2 catalysts.[60–62]

Table 1 The reaction free energy for associative pathways.

	A	B	C	D
ΔG	1.53 eV	1.37 eV	2.47 eV	1.72 eV

Here, we associate the electrochemical step with the highest free energy, $\eta = \max(\Delta G_1, \Delta G_2, \Delta G_3$ and $\Delta G_5)$ as the reaction overpotential, where ΔG_s are calculated using the CHE as described in ref. [56]. We do not consider configurational entropy contribution to the free energy, because we expect it to be small, since the doping levels and the number of possible configurations on 2D active sites are much smaller than on 3D active sites at metal surfaces. In addition to reaction overpotential, we also calculate the thermochemical free energy barrier for O_2 desorption, defined as the difference between the free energy levels of O_2 in the gas phase and O_2 adsorbed on the surface: $\Delta G_b(O_2) = \Delta G(O_2(g)) - \Delta G({}^{*}O_2)$. As aforementioned, desorption of O_2 can become reaction bottleneck in the case $\Delta G_b(O_2)$ is large. The PDS for sites 1, 2 and 3 is Step (1) and for

sites 0, 4, 5 and 6 Step (2). Illustrations of oxygen evolution cycles for sites 1 and 3 showing reaction intermediates along the cycles are presented in Figure 4. It is interesting to note changes in magnetic moments of Mn ions along the reaction path as they can shed more light on the oxidation states of Mn and nature of different intermediates during a reaction cycle. At both sites, the PDS comes from oxidation of *OH to *O, i.e. Step 1. The oxidation of OH should be followed by a concomitant charge transfer from Mn to adsorbed O*. As Mn is already in its stable +4 oxidation state, it will reluctantly release another electron. This results in a partial charge transfer between the Mn and the oxygen adsorbate, which makes $Mn^{+4\text{-}5}$ (μ_{Mn}= 2.60 μ_B) and a partial hole on *O (μ_O = 0.35 μ_B). Also during step 4, the peroxo *OOH converts to an adsorbed superoxo $^{*}O_2^-$,[63] evidenced by shortening of the bond length from 1.43 Å to 1.26 Å. We perform the same analysis on the (100) termination, wherein we identify 4 different sites for oxygen evolution (cf. **Figure 3**b). The reaction overpotentials and desorption barriers at single sites on both terminations are listed in Table **2**, while the free energy values of the different electrochemical steps are given in Note 2 in the ESI.

Table 2 Reaction overpotentials and thermochemical barriers for O_2 desorption at different surface sites.

Sites	η_{OER} [V]		$\Delta G_b(O_2)$ [eV]	
	110	100	110	100
1	0.58	1.09	0.13	-0.57
2	1.07	1.12	0.03	-0.11
3	0.50	0.99	0.21	0.51
4	0.87	1.12	0.39	0.67
5	0.79		0.34	
6	1.61		0.30	

We find that sites 1 and 3 on the (110) termination are the most active sites for oxygen evolution both in terms of η_{OER} and $\Delta G_b(O_2)$. Furthermore, these sites are far more active than any of the sites on the (100) termination, which leads to the conclusion that the (110) facet is generally more active than the (100) facet. Sites 1 and 3 are henceforth referred to as ‘cus’ and ‘bridge’ sites.

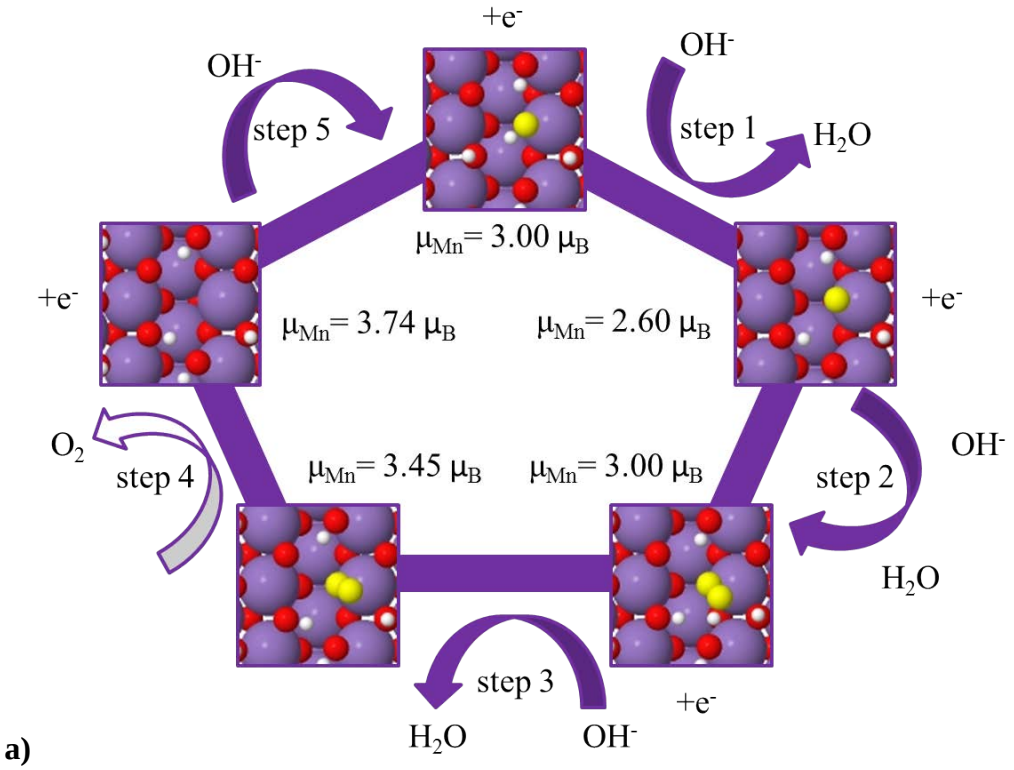

a)

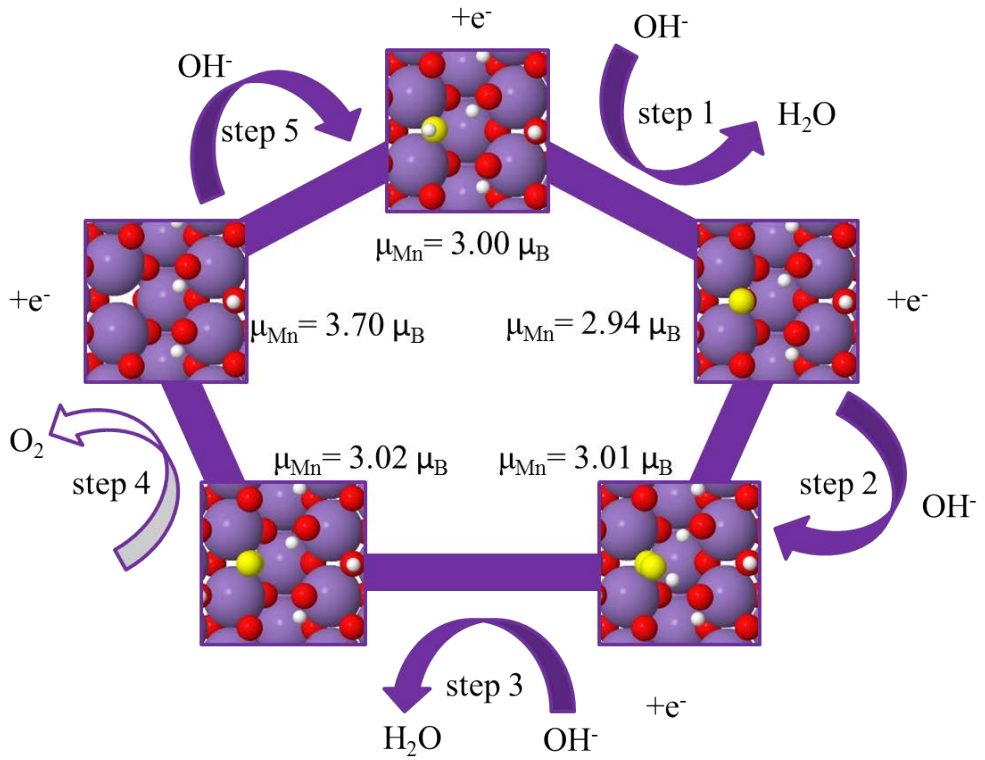

b)

Figure 4 Illustrations of different electro(chemical) steps in a single oxygen evolution cycle at a) cus and b) bridge site on the (110) termination. Steps 1, 2, 3 and 5 are electrochemical steps (filled arrows), whereas step 4 is a chemical step (empty arrows). Oxygen atoms in reaction intermediates are highlighted in yellow.

3.2. Doped

We explore the possibility of enhancing the catalytic performance by means of doping. We limit the analysis on the more active and close-packed (110) termination.

3.2.1. Stability

First, we adjust the dopant ion valence in αMnO_2. We do this in a slightly different manner than for Mn. To recall, for pure Mn we assumed that additional charge is equally distributed over Mn ions that share the same ligand on which the charge was introduced. In the case of dopant atoms, we assume the opposite, namely, that charge is donated/withdrawn from the dopant site only. Consequently, the number of added/removed hydrogen atoms compared to the pure Mn surface is equal to $V_d - 4$, where V_d is the dopant ion valence. Illustrations of the cus and bridge sites on the example of di-(Mg), tri-(Al), tetra-(Pd) and pentavalent (Nb) dopants are shown in **Figure 5**. For Mg and Al, the representative cases of di- and trivalent dopants, we have also investigated whether a second water molecule can dissociate on the surface, in which case OH would sit on-top of a dopant atom (see Note 1 in ESI). However, the free energy difference for water dissociation is found to be endergonic by 1.10 and 0.44 eV, respectively.

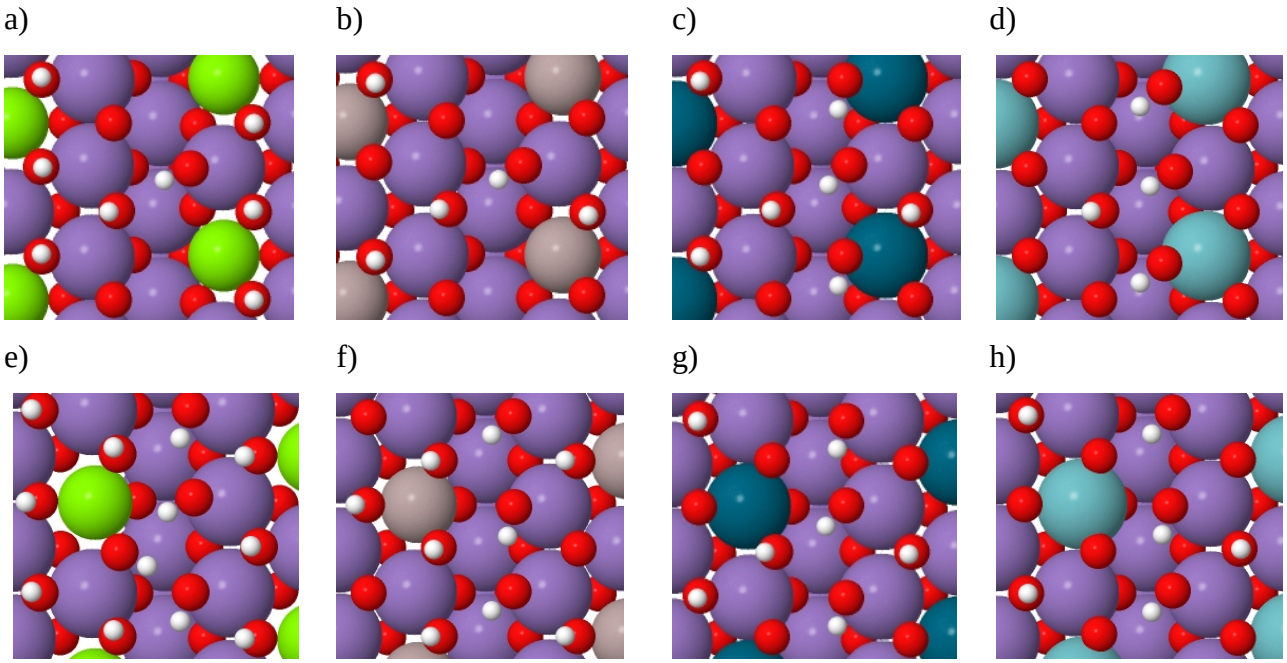

Figure 5 Illustrations of the cus (top) and bridge (bottom) sites on the modified (110) termination for a+e) Mg b+f) Al, c+g) Pd and d+h) Nb doped αMnO_2. Mg, Al, Pd, Nb, Mn, O and H are represented by green, grey, dark blue, turquoise, purple, red and white balls.

Once we calculated the relevant surface terminations, we computed heats of formation for 21 different metal dopants (Cr, Fe, Co, Ni, Cu, Zn, Cd, Mg, Al, Ga, In, Sc, Ru, Rh, Ir, Pd, Pt, Ti, Zr, Nb and Sn) in αMnO_2 compared in **Figure 6**. We employ a tolerance value of +0.3 eV for the stability, thereby assuming that every catalyst whose formation energy is below +0.3 eV is considered stable. This is an arbitrary value which takes inherent errors in the DFT method and the slab model into account. As seen, the bulk site is energetically the least favorable site for Mn substitution. There are in total three dopants (Co, Al and Pd) that favor substitution of Mn at the bulk site, nine (Co, Ni, Mg, Al, Ga, Ru, Pd, Ti and Nb) prefer the cus and twelve (Cr, Fe, Co, Ni, Al, Ga, Sc, Ru, Pd, Pt, Ti and Nb) the bridge site. For the stable subset of catalysts (24), we compute the reaction overpotentials for the OER, together with the free energy barriers for removing O_2 from the surface.

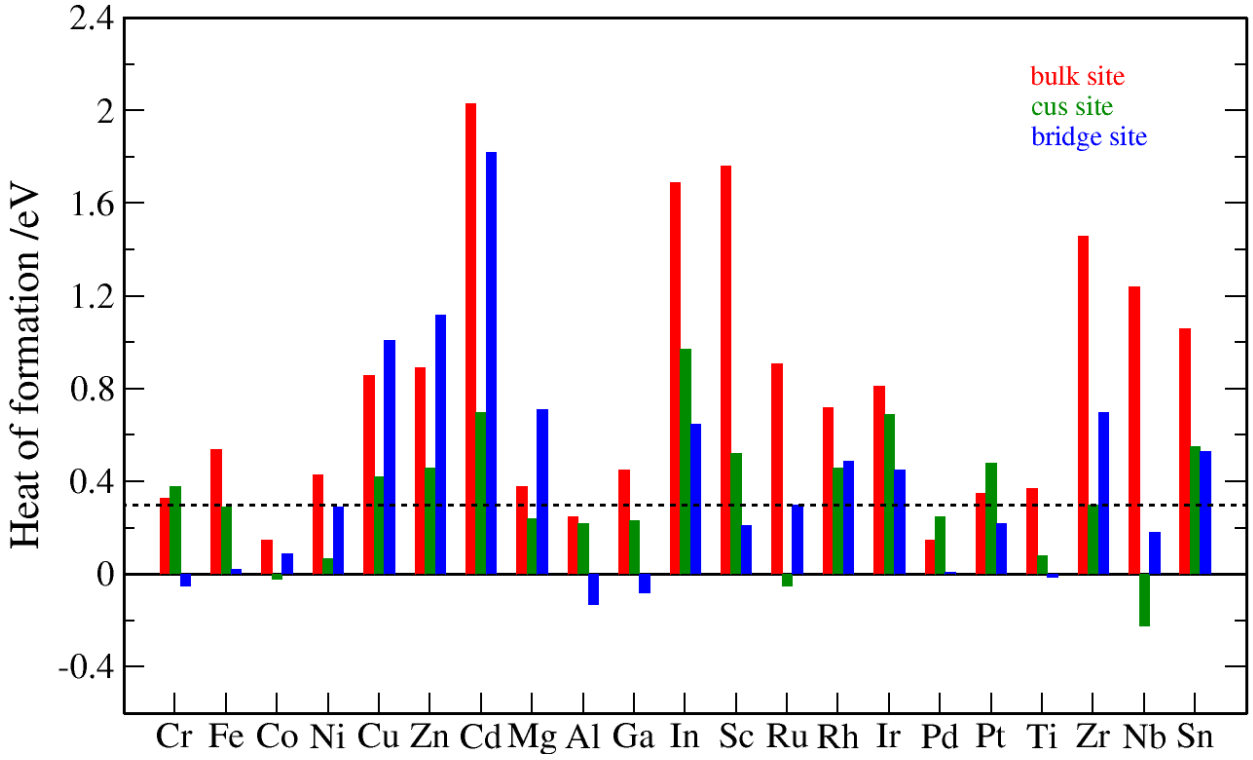

Figure 6 Heats of formation of doped αMnO_2 catalysts at three different sites. Dashed line at 0.3 eV denotes the stability threshold under which all catalysts are considered potentially stable.

3.2.2. Activity

We perform the same analysis on the stable, doped catalysts, where we limit the investigation to the two best sites found on pure (110) αMnO_2. The corresponding η and $\Delta G(O_2(g))$- ΔG ($^*O_2$) are

shown in Figure 7. In the case of first-row TM dopants there are two inequivalent cus sites for evolving oxygen, the Mn and the dopant cus site (cf. **Figure 5**c). For all the other dopants, the reaction can only take place at the Mn site, because metals other than first-row TM cannot easily assume a different oxidation state to accommodate various reaction intermediates. In such systems the difference in η_{OER} comes from changes in the binding energies caused by a nearest neighbor foreign ion. Furthermore, we find that in the presence of 2-fold or 3-fold oxygen vacancies the reduction happens first on the TM dopant ion, which leads to the conclusion that the reduction potentials of Cr^{4+}, Fe^{4+}, Co^{4+} and Ni^{4+} in αMnO_2 are higher than that of Mn^{4+}.

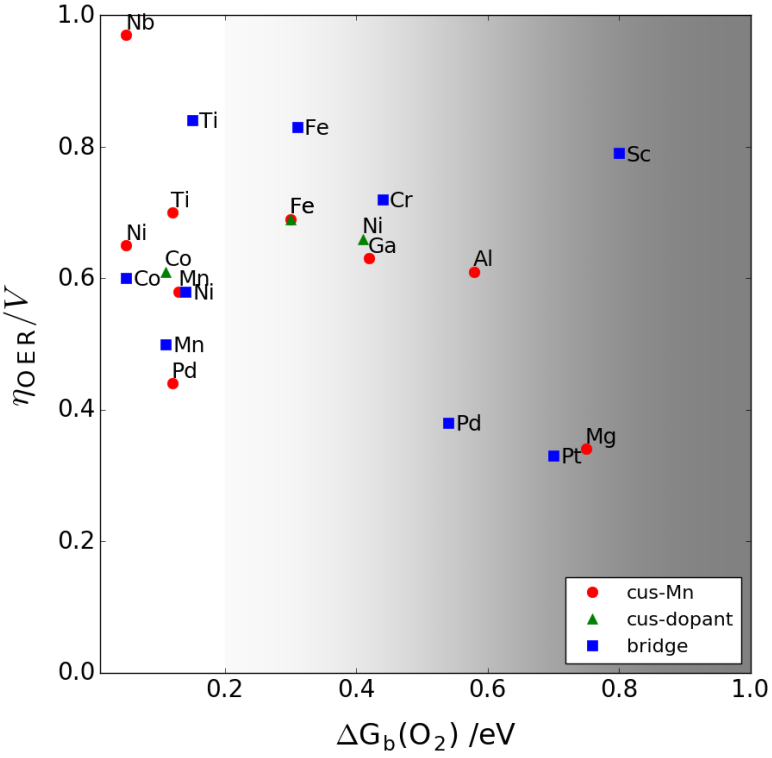

Figure 7 Activity plot showing how reaction overpotential (y-axis) and thermodynamic barrier for O_2 desorption (x-axis) change for different dopants at the cus Mn (red circles), cus dopant (green triangles) and bridge (blue squares) sites. For points under the shaded grey area, the kinetic limiting step will likely be O_2 desorption from the surface.

An ideal catalyst should feature a low η and have a low thermochemical barrier for O_2 desorption. For thermochemical barrier that is surmountable under usual operating conditions, we take a value of 0.2 eV. The activation free energy barrier will expectedly be higher than 0.2 eV because O_2 cannot gain entropy immediately after leaving the surface, which suggests that there will be an entropic barrier on top of the thermochemical barrier for O_2 desorption.[64] The entropy

contribution to the O_2(g) free energy is quite substantial and amounts to 0.64 eV at standard conditions. We have set a gradient starting at 0.2 V to eliminate all catalysts with high O_2 desorption barriers. We find Pd doped αMnO_2 to be the best catalyst and the only material that can outperform pristine αMnO_2. This result agrees very well with recent experimental results, in which a strong interaction of Pd with a MnO_2 substrate has been recognized as the origin of enhanced activity for the OER.[44] The strong interaction does not necessarily imply Pd incorporation into αMnO_2, but rather emphasizes the synergistic effect of Pd and αMnO_2. The beneficial effect of Pd on the OER activity can be better understood through changes in the PDS. The PDS for TM dopants that prefer the +3 oxidation state (Co, Ni[2] and Fe) is Step 5, in which the dopant ion has to oxidize to +4. On the other hand, for Mn and dopants that do not change its oxidation state, the PDS is Step 1, in which the Mn ion should become +5. As Mn does not prefer to be +5, there is a partial hole on $^*O$ (*vide infra*). Oxygen hole can be mitigated by having an electronegative metal next to Mn that can assist Mn oxidation by drawing charge from it. As the oxygen reduction cycle is just opposite to the oxygen reduction cycle, the same oxidation states will likely play a role in the latter reaction as well. This finding might explain why addition of electronegative TM promotes the oxygen reduction rate.[65–67] The free energy values and magnetic moments of Mn and dopant ions in the reaction cycle are given in Note 2 in the ESI.

3.2.3. Electrical conductivity

Finally, we have qualitatively assessed electron conductivities of pure, doped and ion intercalated αMnO_2 by examining the occupation of energy levels in the DOS plots. We find that αMnO_2 is a bulk semiconductor with a band gap of ~1.0 eV and that only Ru, Rh, Ir and Nb dopants have the ability to promote the electronic conduction. Ru, Rh and Ir have broad bands crossing the Fermi level, similarly as in their native rutile oxides. The conduction mechanism in Nb-doped αMnO_2 is of a different origin and stems from charge transfer between Nb and a host Mn ion. As Nb favors the +5 oxidation state, an electron is transferred to a vicinal Mn^{4+}, which becomes Mn^{3+}. The existence of Mn^{4+}/Mn^{3+} ion pairs promotes charge transfer along the Mn^{4+} - O - Mn^{3+} chains *via* polaron hopping. Unfortunately, as neither Ru, Rh, Ir nor Nb are stable in αMnO_2, it will be difficult to improve the bulk conductivity by means of doping. An alternative solution is to intercalate cations from the electrolyte solution inside the 2x2 tunnels. There have been several studies about Li^+ and Zn^{2+} ion intercalation into αMnO_2 for use in Li-ion and Zn-air batteries.[34,68–

[2] Co and Ni dopants were modelled in the -+4 oxidation state.

[70] Intercalation of mono- and divalent cations has the same effect as doping with high valent (>4) elements. Adding Pd and intercalating a cation that does not incorporate into αMnO_2 is expected to both reduce the reaction overpotential and improve the electronic conductivity.

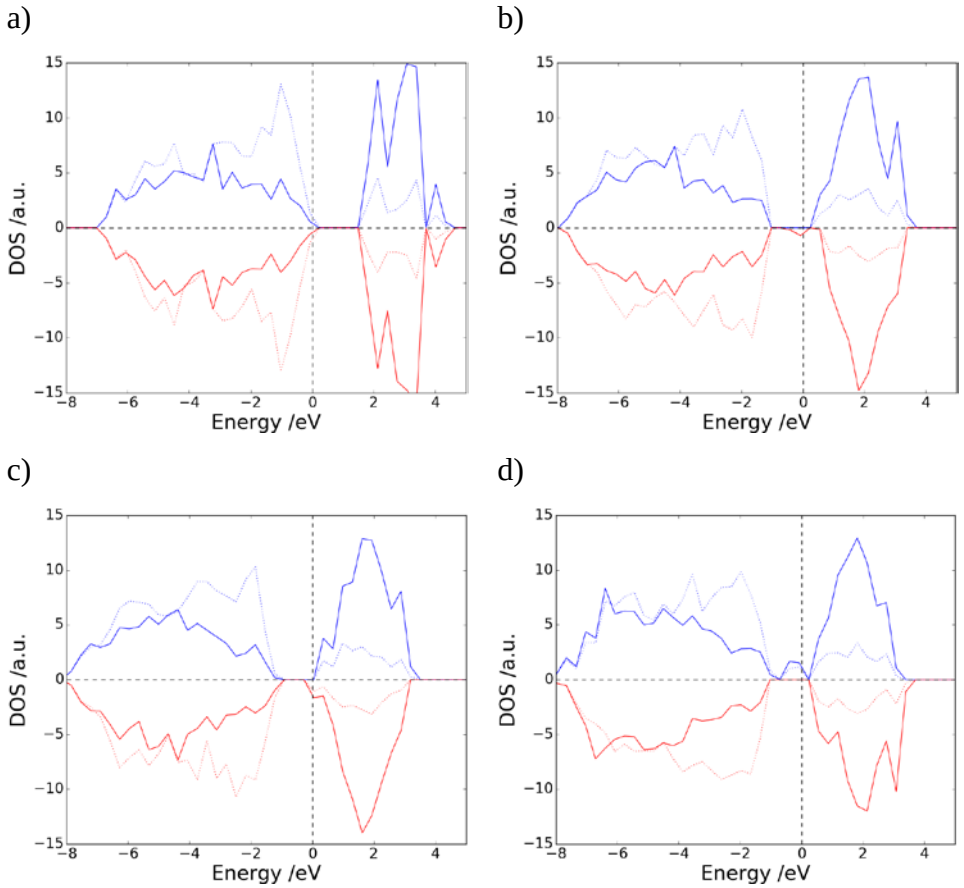

Figure 8 Density of states (DOS) for a) pure b) Nb-doped, c) $2Li^+$ and d) Zn^{2+}-intercalated αMnO_2. Solid lines are the DOS projected onto Mn 3d orbitals and dashed lines are the total DOS (E_{fermi} = 0 eV). Emergence of a polaron state in b and c is discerned by a small shoulder at the conduction band edge.

We expect the conductivity to increase linearly with the concentration and valence of intercalated ions. In **Figure 8**, we compare DOS of the pure, Nb doped, Li^+ and Zn^{2+} intercalated αMnO_2 (see the relaxed structures under Note 3 in ESI). As seen, the pure αMnO_2 is a semiconductor. Doping with pentavalent Nb creates small polaron states at the Fermi level. Similar results are obtained for Li^+ intercalated αMnO_2; the only difference is that the polaron state has merged with the conduction band edge, effectively turning the crystal into an n-doped semiconductor.

4. Conclusions

In summary, we have investigated the structural stability, catalytic activity and electronic conductivity of pure and doped aMnO_2. We summarize the main conclusions in several points.

1. We introduce a simple method to tune the valence of surface metal ions to nominal values by adding/subtracting electrons through addition/removal of hydroxyls and hydrogen atoms. This method is generally applicable, regardless of the surface and can be used whenever the surface oxidation state of an ion is different from its nominal value at given conditions.
2. We find lower reaction overpotentials on a more closely-packed (110) than the (100) surface.
3. We distinguish between three different active sites, cus, bridge and bulk, and find that dopants prefer the surface sites over the bulk site.
4. We consider several reaction mechanisms taking place at single and double sites and find that the former has much lower chemical barriers and reaction overpotentials.
5. From a subset of stable dopants, we identify Pd doped αMnO_2 as the best oxygen evolving electrocatalyst. We ascribe the promoting effect of Pd to its ability to assist Mn oxidation.
6. Dopants that promote bulk electronic conductivity do not incorporate into αMnO_2. An alternative solution to promote conduction is to intercalate mono- or divalent cations.

Acknowledgements

This work was supported by the Horizon 2020 framework project ZAS, grant number 646186. We would also like to acknowledge the Velux Foundations for support through The VILLUM Center for the Science of Sustainable Fuels and Chemicals (grant number 9455).

References

[1] J. K. Nørskov, J. Rossmeisl, A. Logadottir, L. Lindqvist, J. R. Kitchin, T. Bligaard, H. Jonsson, *J. Phys. Chem. B* **2004**, *108*, 17886–17892.

[2] J. Rossmeisl, Z. W. Qu, H. Zhu, G. J. Kroes, J. K. Nørskov, *J. Electroanal. Chem.* **2007**, *607*, 83–89.

[3] X. Zhao, M. Yin, L. Ma, L. Liang, C. P. Liu, J. H. Liao, T. H. Lu, W. Xing, *Energy Environ.*

Sci. **2011**, *4*, 2736–2753.

[4] N. Markovic, H. Gasteiger, P. N. Ross, *J. Electrochem. Soc.* **1997**, *144*, 1591–1597.

[5] B. B. Blizanac, P. N. Ross, N. M. Markovic, *Electrochim. Acta* **2007**, *52*, 2264–2271.

[6] S. Kondo, M. Nakamura, N. Maki, N. Hoshi, *J. Phys. Chem. C* **2009**, *113*, 12625–12628.

[7] F. H. B. Lima, J. Zhang, M. H. Shao, K. Sasaki, M. B. Vukmirovic, E. A. Ticianelli, R. R. Adzic, *J. Phys. Chem. C* **2007**, *111*, 404–410.

[8] C. C. L. McCrory, S. Jung, I. M. Ferrer, S. M. Chatman, J. C. Peters, T. F. Jaramillo, *J. Am. Chem. Soc.* **2015**, *137*, 4347–4357.

[9] F. Song, X. Hu, *Nat. Commun.* **2014**, *5*, 4477.

[10] C. C. L. McCrory, S. Jung, J. C. Peters, T. F. Jaramillo, *J. Am. Chem. Soc.* **2013**, *135*, 16977–87.

[11] S. Jung, C. C. L. McCrory, I. M. Ferrer, J. C. Peters, T. F. Jaramillo, *J. Mater. Chem. A* **2016**, *4*, 3068–3076.

[12] J. Suntivich, K. J. May, H. A. Gasteiger, J. B. Goodenough, Y. Shao-Horn, *Science (80-.).* **2011**, *334*, 1383–1385.

[13] M. Huynh, C. Shi, S. J. L. Billinge, D. G. Nocera, *J. Am. Chem. Soc.* **2015**, *137*, 14887–14904.

[14] Y. Gorlin, B. Lassalle-Kaiser, J. D. Benck, S. Gul, S. M. Webb, V. K. Yachandra, J. Yano, T. F. Jaramillo, *J. Am. Chem. Soc.* **2013**, *135*, 8525–8534.

[15] K. N. Ferreira, T. M. Iverson, K. Maghlaoui, J. Barber, S. Iwata, *Science (80-.).* **2004**, *303*, 1831–1838.

[16] J. E. Post, *Proc. Natl. Acad. Sci.* **1999**, *96*, 3447–3454.

[17] M. Pourbaix, *Atlas of Electrochemical Equilibria in Aqueous Solutions*, National Association Of Corrosion Engineers, Houston, Texas, **1974**.

[18] P. Atkins, *Physical Chemistry*, W.H. Freemen & Company, **1997**.

[19] S. Fritsch, J. E. Post, A. Navrotsky, *Geochim. Cosmochim. Acta* **1997**, *61*, 2613–2616.

[20] D. A. Kitchaev, H. Peng, Y. Liu, J. Sun, J. P. Perdew, G. Ceder, *Phys. Rev. B* **2016**, *93*, 45132.

[21] A. I. Khan, D. O'Hare, R. J. Francis, D. O'Hare, R. I. Smith, R. Done, R. J. Humphreys, S. M. Clark, G. N. Greaves, *J. Mater. Chem.* **2002**, *12*, 3191–3198.

[22] V. Tripkovic, H. A. Hansen, T. Vegge, *ACS Catal.* **2017**, acscatal.7b02712.

[23] Y. Meng, W. Song, H. Huang, Z. Ren, S.-Y. Chen, S. L. Suib, *J. Am. Chem. Soc.* **2014**, *136*, 11452–64.

[24] G.-Q. Han, Y.-R. Liu, W.-H. Hu, B. Dong, X. Li, X. Shang, Y.-M. Chai, Y.-Q. Liu, C.-G. Liu, *J. Electrochem. Soc.* **2016**, *163*, H67–H73.

[25] K. Selvakumar, S. M. Senthil Kumar, R. Thangamuthu, G. Kruthika, P. Murugan, *Int. J. Hydrogen Energy* **2014**, *39*, 21024–21036.

[26] J.-K. Chang, M.-T. Lee, W.-T. Tsai, *J. Power Sources* **2007**, *166*, 590–594.

[27] H.-Y. Su, Y. Gorlin, I. C. Man, F. Calle-Vallejo, J. K. Norskov, T. F. Jaramillo, J. Rossmeisl, *Phys. Chem. Chem. Phys.* **2012**, *14*, 14010–14022.

[28] F. Cheng, Y. Su, J. Liang, Z. Tao, J. Chen, *Chem. Mater.* **2010**, *22*, 898–905.

[29] K. A. Stoerzinger, M. Risch, B. Han, Y. Shao-Horn, *ACS Catal.* **2015**, *5*, 6021–6031.

[30] E. M. Benbow, S. P. Kelly, L. Zhao, J. W. Reutenauer, S. L. Suib, *J. Phys. Chem. C* **2011**, *115*, 22009–22017.

[31] Y. L. Cao, H. X. Yang, X. P. Ai, L. F. Xiao, *J. Electroanal. Chem.* **2003**, *557*, 127–134.

[32] H. Jiang, C. Li, T. Sun, J. Ma, *Nanoscale* **2012**, *4*, 807–812.

[33] L. Hu, W. Chen, X. Xie, N. Liu, Y. Yang, H. Wu, Y. Yao, M. Pasta, H. N. Alshareef, Y. Cui, *ACS Nano* **2011**, *5*, 8904–8913.

[34] A. Débart, A. J. Paterson, J. Bao, P. G. Bruce, *Angew. Chemie Int. Ed.* **2008**, *47*, 4521–4524.

[35] D. A. Tompsett, S. C. Parker, M. S. Islam, *J. Mater. Chem. A* **2014**, *2*, 15509.

[36] D. M. Robinson, Y. B. Go, M. Mui, G. Gardner, Z. Zhang, D. Mastrogiovanni, E. Garfunkel, J. Li, M. Greenblatt, G. C. Dismukes, *J. Am. Chem. Soc.* **2013**, *135*, 3494–3501.

[37] X. Li, J. Liu, Y. Zhao, H. Zhang, F. Du, C. Lin, T. Zhao, Y. Sun, *ChemCatChem* **2015**, *7*, 1848–1856.

[38] P. F. Smith, B. J. Deibert, S. Kaushik, G. Gardner, S. Hwang, H. Wang, J. F. Al-Sharab, E. Garfunkel, L. Fabris, J. Li, et al., *ACS Catal.* **2016**, *6*, 2089–2099.

[39] I. Zaharieva, P. Chernev, M. Risch, K. Klingan, M. Kohlhoff, A. Fischer, H. Dau, *Energy Environ. Sci.* **2012**, *5*, 7081–7089.

[40] J. Du, T. Zhang, F. Cheng, W. Chu, Z. Wu, J. Chen, *Inorg. Chem.* **2014**, *53*, 9106–14.

[41] J. Suntivich, H. A. Gasteiger, N. Yabuuchi, H. Nakanishi, J. B. Goodenough, Y. Shao-Horn, *Nat. Chem.* **2011**, *3*, 546–550.

[42] K. A. Stoerzinger, W. Lü, C. Li, Ariando, T. Venkatesan, Y. Shao-Horn, *J. Phys. Chem. Lett.* **2015**, *6*, 1435–1440.

[43] C.-H. Kuo, W. Li, L. Pahalagedara, A. M. El-Sawy, D. Kriz, N. Genz, C. Guild, T. Ressler, S. L. Suib, J. He, *Angew. Chem. Int. Ed. Engl.* **2015**, *54*, 2345–50.

[44] J.-H. Zhang, J.-Y. Feng, T. Zhu, Z.-L. Liu, Q.-Y. Li, S.-Z. Chen, C.-W. Xu, *Electrochim. Acta* **2016**, *196*, 661–669.

[45] J. Luo, H. T. Zhu, J. K. Liang, G. H. Rao, J. B. Li, Z. M. Du, *J. Phys. Chem. C* **2010**, *114*, 8782–8786.

[46] M. J. Young, A. M. Holder, S. M. George, C. B. Musgrave, *Chem. Mater.* **2015**, *27*, 1172–1180.

[47] R. Younesi, A. Christiansen, S. Loftager, J. M. García-Lastra, T. Vegge, P. Norby, P. Holtappels, *ChemSusChem* **2015**, *8*, 3213–3216.

[48] L. Li, X. Feng, Y. Nie, S. Chen, F. Shi, K. Xiong, W. Ding, X. Qi, J. Hu, Z. Wei, et al., *ACS Catal.* **2015**, *5*, 4825–4832.

[49] G. Kresse, J. Furthmüller, *Phys. Rev. B* **1996**, *54*, 11169–11186.

[50] J. P. Perdew, K. Burke, M. Ernzerhof, *Phys. Rev. Lett.* **1996**, *77*, 3865–3868.

[51] S. L. Dudarev, G. A. Botton, S. Y. Savrasov, C. J. Humphreys, A. P. Sutton, **1997**.

[52] H. A. Hansen, I. C. Man, F. Studt, F. Abild-Pedersen, T. Bligaard, J. Rossmeisl, *Phys. Chem. Chem. Phys.* **2009**, *12*, 283–290.

[53] A. Ramírez, P. Hillebrand, D. Stellmach, M. M. May, P. Bogdanoff, S. Fiechter, *J. Phys. Chem. C* **2014**, *118*, 14073–14081.

[54] R. Christensen, H. A. Hansen, C. F. Dickens, J. K. N?rskov, T. Vegge, *J. Phys. Chem. C* **2016**, *120*, 24910–24916.

[55] V. Tripkovic, E. Skúlason, S. Siahrostami, J. K. Nørskov, J. Rossmeisl, *Electrochim. Acta* **2010**, *55*, 7975–7981.

[56] J. Rossmeisl, Z.-W. Qu, H. Zhu, G.-J. Kroes, J. K. Nørskov, *J. Electroanal. Chem.* **2007**, *607*, 83–89.

[57] V. Tripkovic, H. A. Hansen, J. Rossmeisl, T. Vegge, *Phys. Chem. Chem. Phys.* **2015**, *17*, 11647–57.

[58] T. Tripkovic, V.; Vegge, *J. Phys. Chem. C* **2017**.

[59] H. A. Hansen, V. Viswanathan, J. K. Nørskov, *J. Phys. Chem. C* **2014**, *118*, 6706–6718.

[60] M. S. El-Deab, T. Ohsaka, *Angew. Chemie Int. Ed.* **2006**, *45*, 5963–5966.

[61] I. Roche, E. Chaînet, M. Chatenet, J. Vondrák, *J. Phys. Chem. C* **2007**, *111*, 1434–1443.

[62] F. H. B. Lima, M. L. Calegaro, E. A. Ticianelli, *Electrochim. Acta* **2007**, *52*, 3732–3738.

[63] R. R. Rao, M. J. Kolb, N. B. Halck, A. F. Pedersen, A. Mehta, H. You, K. A. Stoerzinger, Z. Feng, H. A. Hansen, H. Zhou, et al., *Energy Environ. Sci.* **2017**, DOI 10.1039/C7EE02307C.

[64] J. Rossmeisl, K. Chan, E. Skúlason, M. E. Björketun, V. Tripkovic, *Catal. Today* **2016**, *262*, 36–40.

[65] L. Wei, C. Li, H. Chu, Y. Li, *Dalt. Trans.* **2011**, *40*, 2332–2337.

[66] Q. Tang, L. Jiang, J. Qi, Q. Jiang, S. Wang, G. Sun, *Appl. Catal. B Environ.* **2011**, *104*, 337–

345.

[67] W. Sun, A. Hsu, R. Chen, *J. Power Sources* **2011**, *196*, 4491–4498.

[68] † Benxia Li, † Guoxin Rong, *,† Yi Xie, ‡ and Lunfeng Huang, C. Feng‡, **2006**, DOI 10.1021/IC0606274.

[69] R. Guduru, J. Icaza, *Nanomaterials* **2016**, *6*, 41.

[70] C. Xu, B. Li, H. Du, F. Kang, *Angew. Chemie Int. Ed.* **2012**, *51*, 933–935.